Elucidation of the Local and Long-Range Structural Changes that Occur in Germanium Anodes in Lithium-Ion Batteries

Hyeyoung Jung,[†] Phoebe K. Allan,[‡,§] Yan-Yan Hu,[‡] Olaf J. Borkiewicz,[∥] Xiao-Liang Wang,[⊥] Wei-Qiang Han,[⊥] Lin-Shu Du,[†] Chris J. Pickard,[#] Peter J. Chupas,[∥] Karena W. Chapman,[∥] Andrew J. Morris,[∇] and Clare P. Grey*,[†,‡]

[†]Department of Chemistry, Stony Brook University, Stony Brook, New York 11794, United States

[‡]Department of Chemistry, University of Cambridge, Lensfield Road, Cambridge CB2 1EW, U.K.

[§]Gonville and Caius College, Cambridge CB2 1TA, U.K.

[∥]X-ray Science Division, Advanced Photon Source, Argonne National Laboratory, Argonne, Illinois 60439, United States

[⊥]Ningbo Institute of Materials Technology & Engineering (NIMTE), Chinese Academy of Sciences, Ningbo 315201, P. R. China

[#]Department of Physics and Astronomy, University College London, Gower Street, London WC1E 6BT, U.K.

[∇]Theory of Condensed Matter Group, Cavendish Laboratory, University of Cambridge, J. J. Thomson Avenue, Cambridge CB3 0HE, U.K.

S *Supporting Information*

ABSTRACT: Metallic germanium is a promising anode material in secondary lithium-ion batteries (LIBs) due to its high theoretical capacity (1623 mAh/g) and low operating voltage, coupled with the high lithium-ion diffusivity and electronic conductivity of lithiated Ge. Here, the lithiation mechanism of micron-sized Ge anodes has been investigated with X-ray diffraction (XRD), pair distribution function (PDF) analysis, and *in-/ex-situ* high-resolution ^7Li solid-state nuclear magnetic resonance (NMR), utilizing the structural information and spectroscopic fingerprints obtained by characterizing a series of relevant Li_xGe_y model compounds. In contrast to previous work, which postulated the formation of Li_9Ge_4 upon initial lithiation, we show that crystalline Ge first reacts to form a mixture of amorphous and crystalline Li_7Ge_3 (space group $P3_21$). Although Li_7Ge_3 was proposed

to be stable in a recent theoretical study of the Li−Ge phase diagram (Morris, A. J.; Grey, C. P.; Pickard, C. J. *Phys. Rev. B: Condens. Matter Mater. Phys.* **2014**, *90*, 054111), it had not been identified in prior experimental studies. Further lithiation results in the transformation of Li_7Ge_3, via a series of disordered phases with related structural motifs, to form a phase that locally resembles Li_7Ge_2, a process that involves the gradual breakage of the Ge−Ge bonds in the Ge−Ge dimers (dumbbells) on lithiation. Crystalline $Li_{15}Ge_4$ then grows, with an overlithiated phase, $Li_{15+δ}Ge_4$, being formed at the end of discharge. This study provides comprehensive experimental evidence, by using techniques that probe short-, medium-, and long-range order, for the structural transformations that occur on electrochemical lithiation of Ge; the results are consistent with corresponding theoretical studies regarding stable lithiated Li_xGe_y phases.
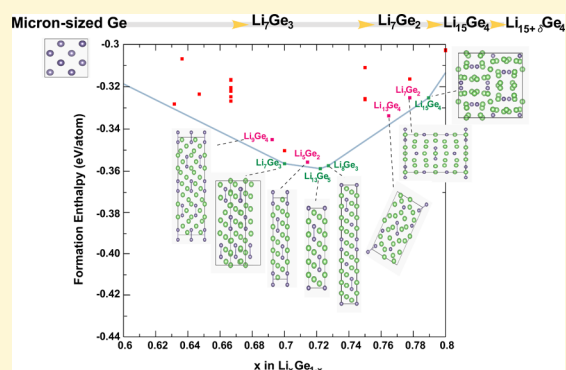
1. INTRODUCTION

Lithium-ion batteries (LIBs) are the current leading technology for electrochemical energy storage and are widely used in portable electronics. The rapidly growing demand for LIBs for use in electric vehicles and large-scale energy storage systems necessitates the search for new electrode materials with higher power and increased energy densities.[1] Silicon, germanium, and tin are attractive anode materials for LIBs due to their high energy densities.[2] These elements undergo alloying processes with Li and exhibit much higher theoretical capacities—3579, 1623, and 993 mAh/g for silicon, germanium, and tin, respectively—compared with graphite (375 mAh/g),[3,4] driving the capacity toward that achievable by using lithium−metal

anodes while mitigating some of the safety issues.[5] The bulk of research has been focused on silicon anodes because they show the highest capacity among all anode materials except Li metal, with Si also having high natural abundance and low cost. In contrast, the more expensive germanium anode has received little attention. However, the lithium diffusivity in bulk Ge is 400 times higher than the lithium diffusivity in Si,[6] and the electronic conductivity of Ge is 2 orders of magnitude larger than Si due to its smaller band gap ($E_g(Ge)$ = 0.6 eV vs $E_g(Si)$

= 1.1 eV).[7] These properties lead to far superior rate performance for Ge anodes than Si anodes in LIBs.[8]

Sangster et al. reported a binary phase diagram of the Li−Ge system consisting of seven experimentally reported crystalline phases: Li_7Ge_{12}, LiGe, $Li_{11}Ge_6$, Li_9Ge_4, Li_7Ge_2, $Li_{15}Ge_4$, and $Li_{22}Ge_5$.[9] In addition, $Li_{14}Ge_6$ (Li_7Ge_3) and $Li_{12}Ge_7$[10−13] have been reported. Recent DFT calculations by some of us have shown that the Li−Ge phase diagram is extremely rich. LiGe($I4_1/a$), Li_7Ge_3 ($P32_12$), $Li_{13}Ge_5$($P\bar{3}m1$), Li_8Ge_3($R\bar{3}m$), $Li_{15}Ge_4$($I\bar{4}3d$), and $Li_{17}Ge_4$($F\bar{4}3m$) were identified via the combined random structure searching[14,15] and atomic species swapping methods[16] to be stable (i.e., lie on a convex hull between Li and Ge), while other Li_xGe_y alloys, including Li_5Ge_2 and $Li_{13}Ge_4$,[16] are only slightly metastable with respect to disproportionation to the thermodynamic phases and hence, are likely to be also present at room temperature.

Several papers have studied the reactions of Ge in a LIB. St. John et al.[17] reported five distinct two-phase plateaus in the discharge and charge electrochemical profiles of molten salt Ge−Li batteries between 360 and 440 °C and associated these plateaus with the formation of LiGe, Li_9Ge_4, $Li_{16}Ge_5$, $Li_{15}Ge_4$, and $Li_{22}Ge_5$, respectively. By analogy with Si,[18,19] Ge may follow a different electrochemical lithiation pathway at room temperature, possibly involving the formation of metastable and amorphous phases. A number of mechanistic studies on the electrochemical lithiation process of Ge anodes at room temperature have been reported, but no consensus on the lithiated phase formed has been reached. Several authors report the formation of $Li_{15}Ge_4$ at the end of lithiation,[20−23] analogous to the final phase formed on fully discharging a silicon electrode.[18,24,25] However, $Li_{22}Ge_5$ has also been reported to form at the end of lithiation.[26,27] Graetz et al.,[26] in an *ex-situ* X-ray diffraction (XRD) study of a thin-film Ge electrode, identified the Li−Ge crystallographic phases LiGe, Li_7Ge_2, and $Li_{15}Ge_4$, and also suggested that $Li_{11}Ge_6$, Li_9Ge_4, and $Li_{22}Ge_5$ may also form in small quantities during the electrode reactions. An *ex-situ* XRD study of an electrochemically lithiated Ge metal electrode by Kim et al.[20] indicated that $Li_{15}Ge_4$ was formed at the end of discharge. Yoon et al.[27] reported a three-step lithiation mechanism (Ge → Li_9Ge_4 → Li_7Ge_2 → $Li_{15}Ge_4$ + $Li_{22}Ge_5$) for a carbon-coated germanium composite electrode based on *ex-situ* XRD and HRTEM analyses. An *in-situ* XRD analysis of lithiated Ge films prepared by both evaporation and sputtering methods by Baggetto et al.[21] indicated that the lithiation process occurred via the formation of a series of amorphous Li−Ge intermediates, eventually forming the fully lithiated product crystalline $Li_{15}Ge_4$. Liu et al.[22] investigated Ge nanowire electrodes by means of *in-situ* TEM and proposed a two-step lithiation process: Ge → amorphous Li_xGe → crystalline $Li_{15}Ge_4$. Finally, more recent *in-situ* XRD and X-ray absorption spectroscopy (XAS) studies[23] suggested that micron-sized crystalline Ge particles are initially converted into an amorphous phase, locally resembling Li_9Ge_4, "a-Li_9Ge_4". Subsequently, the residual crystalline Ge forms amorphous Ge and amorphous Li_xGe phases (mixture of a-Li_9Ge_4, a-LiGe, and a-Li_7Ge_2), and eventually crystalline $Li_{15}Ge_4$.

The crystal structures of a series of Li_xGe_y compounds, relevant to this study, are shown in Figure 1. The phase Li_9Ge_4 (or $Li_{2.25}Ge$), proposed to form in some previous electrochemical studies[23,27] (space group, Cmcm), contains Ge−Ge dumbbells with a Ge−Ge bond length of ∼2.44 Å, with the dumbbells being separated by 2 or 7 Li atoms in rows along the
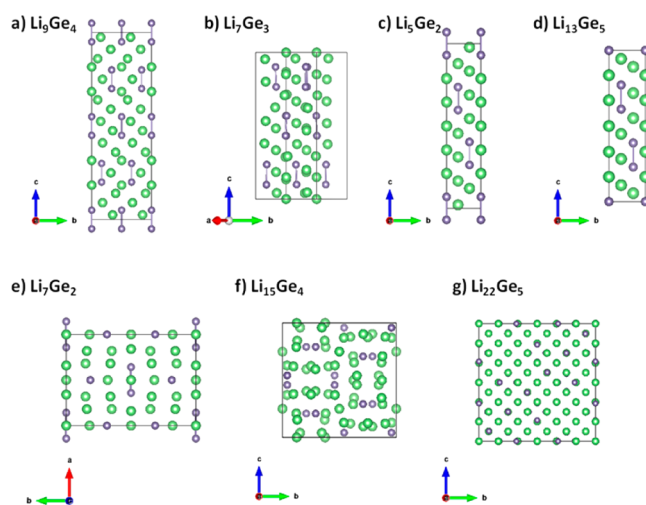
Figure 1. Structures of key Li_xGe crystalline phases investigated as part of this work: (a) Li_9Ge_4 ($Li_{2.25}Ge$, space group, Cmcm, PDF#01-073-6200[30]); (b) Li_7Ge_3 ($Li_{2.33}Ge$, $P32_12$);[16] (c) Li_5Ge_2 ($Li_{2.5}Ge$, $R\bar{3}m$);[16] (d) $Li_{13}Ge_5$ ($Li_{2.6}Ge$, $P\bar{3}m1$);[16] (e) Li_7Ge_2 ($Li_{3.5}Ge$, Cmmm, PDF#00-029-0636[28]); (f) $Li_{15}Ge_4$ ($Li_{3.75}Ge$, $I\bar{4}3d$, PDF#01-089-3034[31]); (g) $Li_{22}Ge_5$ ($Li_{4.4}Ge$, $F\bar{4}3m$, PDF#00-017-0402[32]). Green and blue spheres denote Li and Ge atoms, respectively, with the blue lines indicating Ge−Ge bonds in the Ge dumbbells.

c-axis. The dumbbell columnellar motif is common to Li_xGe_y structures with similar compositions. Li_7Ge_3 (or $Li_{2.33}Ge$), a stable phase identified in our prior DFT studies, adopts the $P32_12$ space group with 8 Li and 3 Ge crystallographic sites.[11] The Ge atoms also form Ge−Ge dumbbells with a Ge−Ge distance of 2.50 Å, with the dumbbells being separated by either 4 or 5 Li atoms along the c-axis. Li_5Ge_2 (or $Li_{2.5}Ge$), another phase identified by DFT, is above the tie-line (i.e., is metastable) and has a $R\bar{3}m$ symmetry with 3 Li and 1 Ge crystallographic sites. The Ge atoms again exist as Ge−Ge dumbbells (Ge−Ge bond distance of 2.56 Å), separated by 5 Li atoms along the c-axis.[16] $Li_{13}Ge_5$ (or $Li_{2.6}Ge$) is a thermodynamically stable phase (on the basis of the DFT studies) with $P\bar{3}m1$ symmetry and 7 Li and 3 Ge crystallographic sites. The isolated Ge atoms in this material are separated by 5 Li atoms, while the Ge−Ge dumbbells with a bond distance of 2.55 Å are separated by 4 Li atoms along the c-axis.[16] Two different polymorphs for Li_7Ge_2 have been suggested by theoretical studies, with symmetries of Cmmm and $P\bar{3}m1$.[16,27,28] However, only the Cmmm structure has been reported experimentally,[27,28] containing Ge−Ge dumbbells and isolated Ge atoms, with 50% of the Ge atoms being present as dumbbells. The structure comprises columns along the a-axis in the crystal structure; one-sixth of these columns contain Ge−Ge dumbbells (with bond length 2.62 Å) separated by one Li atom, while one-third of the columns contain isolated Ge with 2 Li atoms in between, with the rest of the columns containing only Li atoms. Two lithium−germanium alloys with high-lithium content have been reported experimentally: $Li_{15}Ge_4$ (space group: $I\bar{4}3d$) and $Li_{22}Ge_5$ (symmetry group: $F\bar{4}3m$), both containing isolated Ge atoms in a matrix of Li.[12,27,29]

Given the complexity of the phase diagram and the uncertainties of the nature of some of the crystalline and amorphous phases formed, it is clear that further structural elucidation is required, with a focus on techniques that are able to characterize any amorphous or disordered intermediates. In this paper, we probe the structure of Ge-anodes at various

stages of lithiation using *ex-situ* XRD, X-ray pair-distribution function (PDF) analysis, and *in-* and *ex-situ* [7]Li solid-state nuclear magnetic resonance (NMR) spectroscopy. PDF analysis utilizes the total scattering from the sample, treating the diffuse scattering and Bragg scattering in parallel. Thus, while any long-range order is accounted for in the analysis, its presence is not required to obtain structural information. It is, therefore, a particularly powerful technique for characterizing materials in which there is a considerable degree of disorder. Since the intensity of peaks in the PDF is weighted by the scattering amplitude of the atoms in each pair of atoms, PDF analysis of X-ray data is particularly sensitive to Ge connectivity (Ge−Ge and Ge−Li bonding) in the electrodes. *In-* and *ex-situ* solid-state ^{7}Li NMR experiments are employed here to help identify the local structures formed in disordered phases, the method having been shown to be highly sensitive to local structure and deviations from stoichiometry of the crystalline phases in the lithium−silicon system.[18,19,33] The one previous ^{7}Li NMR report of the germanide, $Li_{12}Ge_7$, suggests that ^{7}Li NMR of these systems will be similarly sensitive to local structure and lithium dynamics.[13]

Relevant Li−Ge model compounds (with nominal compositions Li_9Ge_4, Li_7Ge_2, $Li_{15}Ge_4$, and $Li_{22}Ge_5$) have been synthesized and characterized by XRD, solid-state NMR, and PDF analysis to assist with the identification and structural determination of the Li_xGe_y phases that form during electrochemical lithiation. Through the amalgamation of short-range and long-range structural information, we obtain a detailed structural model for how micron-sized germanium particles react to form a series of lithiated germanides, with the final lithiation product corresponding to $Li_{15+x}Ge_4$.

2. EXPERIMENTAL SECTION

2.1. Synthesis of Model Compounds. The lithium−germanium model compounds (with nominal stoichiometries, Li_9Ge_4, Li_7Ge_2, $Li_{15}Ge_4$, and $Li_{22}Ge_5$) were prepared by mechanical mixing. Stoichiometric amounts of lithium foil (Aldrich) and germanium metal (Alfa Aesar, 100 mesh, 99.999%) were mixed in a stainless steel ball-mill jar in an Ar-filled glovebox and ball-milled for 8 h in a SPEX SamplePrep8000 Mixer/Mill high energy ball-mill. The final products were stored under Argon atmosphere before characterization.

2.2. Synthesis of Micron-Sized Germanium. Micron-sized Ge powders were prepared by a 2-step procedure. GeO_2 nanoparticles were first prepared via hydrolysis of $GeCl_4$.[4] 2 mL $GeCl_4$ (99.99%, Alfa Aesar) was added to 8 mL anhydrous ethanol (99.9%, Sigma-Aldrich) and the mixture was stirred for 10 min. In a separate beaker, 10 mL deionized water was added to 100 mL anhydrous ethanol and stirred for 10 min. The $GeCl_4$ mixture was dropped into the water/ethanol solution and stirred continuously for 3 h. The resulting powder was collected by centrifugation, washed with ethanol and dried at 100 °C under air to obtain the final product GeO_2.

The GeO_2 was subsequently reduced under hydrogen gas at 700 °C for 30 min to obtain metallic micron-sized germanium.[34] The synthesized Ge particles were examined by SEM, as seen in Figure S1. The larger spherical Ge particles are made up of 1−3 μm-sized primary particles.

2.3. Electrochemistry. Electrochemically cycled electrode samples for *ex-situ* experiments (NMR, PDF) were prepared using CR 2032-type coin cells. The positive electrodes were formulated from 80% germanium powder as the active material, 10% Super P (Timcal) as a conducting matrix, and 10% polyvinylidene fluoride (PVDF, Kynar Flex 2801-00) as a binder. The mixture was suspended in *N*-methylpyrrolidinone (NMP, 99+% Sigma-Aldrich) to form a slurry; the slurry was then coated on a Cu foil, dried at 100 °C for 10 min in a convection oven (Grieve co.) and then at 60 °C for 24 h in a vacuum oven (Thermo scientific). Coin cells were assembled in an Ar-filled

glovebox using Li metal foil as the negative electrode. 1 M $LiPF_6$ in a 1:1 volumetric mixture of ethylene carbonate (EC) and dimethyl carbonate (DMC) was used as the electrolyte and a porous glass fiber (GF/B, Whatman) as the separator. The cells were cycled using an Arbin instruments battery cycler with a cycling rate of C/50 (corresponding to a discharge to a theoretical capacity of 1623 mAh/g in 50 h, assuming that $Li_{4.4}Ge$ is the final electrochemical lithiation product[26]) between 0.0 to 2.0 V at room temperature. After electrochemical cycling, each cell was dissembled and the active material was washed with dimethyl carbonate (DMC, 99+% Sigma-Alrich) and dried in the Ar-filled glovebox.

For *in-situ* NMR experiments, a flexible battery design was used. The positive electrodes were prepared by mixing 70% germanium, 10% super P, 20% polyvinylidene fluoride (PVDF), and dibutyl phthalate (DBP, 99% Sigma-Aldrich). The mixture was stirred in acetone (99%. J.T. Baker) and spread onto a flat glass surface and dried in air. DBP was removed by washing the film with ether (99%, Sigma-Aldrich). The dried film (4 mm (width) X 10 mm (length)) was laminated onto a carbon-coated Cu mesh and used as the positive electrode. Lithium metal foil of the same dimensions as the positive electrode film was pressed onto Cu wire mesh and used as the negative electrode. 1 M $LiPF_6$ in a 1:1 volumetric mixture of ethylene carbonate (EC) and dimethyl ethyl carbonate (DMC) was used as the electrolyte and a piece of porous glass fiber as the separator. Components were assembled and sealed in a plastic bag (Kapak Corporation, type 500) inside the glovebox. This flexible plastic battery cell was placed in a 5 mm diameter NMR coil of a static probe inside the magnet and connected with the external battery cycler. A Bio-Logic Science Instruments VSP potentiostat/galvanostat was used to electrochemically cycle the bag-cell battery within the voltage window of 0.0−2.0 V.

2.4. X-ray Diffraction. Diffraction patterns were measured on a Bruker D8 diffractometer using Cu K_α irradiation ($\lambda = 1.54$ Å) with a scan rate of 3°/min from a 2θ range of 10° to 80°. Samples were sealed with an airtight cover under Ar atmosphere before being loaded into a XRD holder.

2.5. *Ex-Situ* Pair Distribution Function Analysis. Dried *ex-situ* battery samples for PDF analysis were loaded into 1 mm diameter Kapton capillaries in an Ar-filled glovebox and sealed with epoxy. The samples were then shipped to the Advanced Photon Source (APS), Argonne National Laboratory for measurement, resulting in a time lag up to 2 weeks between sample preparation and acquisition of the total scattering data at the dedicated PDF beamline 11-ID-B at the APS. High-energy X-rays (~58 keV, $\lambda = 0.2128$ Å) were used in combination with a large amorphous-silicon based area detector (PerkinElmer) to collect X-ray scattering data to high values of momentum transfer ($Q_{max} \approx 23$ Å). The scattering images were reduced to one-dimensional data within FIT2D[32] using CeO_2 as a calibration standard. The data were corrected for background scattering, Compton scattering and detector effects within pdfgetX2 and Fourier transformed to get $G(r)$, the PDF. No attempt was made to subtract the carbon signals from the total PDF pattern. Least-squares refinements of structures against PDF data were performed in PDFGui in the distance range of 0−30 Å.[35] The initial value for the Q_{damp} parameter was set as 0.045 and refined against the data for crystalline Ge, and the atomic displacement parameters were set to initial values of $U_{11} = U_{22} = U_{33} = 0.005$ Å^2 (constrained to be equal for all the Ge and Li atoms) and $U_{12} = U_{23} = U_{13} = 0$. Q_{damp}, lattice parameters, the linear atomic correlation factor (delta 1), and anisotropic temperature factors (U_{11}, U_{22}, U_{33}) were refined. The initial refinements of each PDF pattern assume a single pure phase, however, incorporation of a second minor phase significantly improved the refinement quality of some patterns, as indicated by reduced refinement quality factors, i.e., the R_w values. Note that the value of R_w-factors for PDF refinements are higher than those for a Rietveld refinement of similar merit.

2.6. *Ex-Situ* ^{7}Li MAS NMR. *Ex-situ* battery samples were packed in 1.3 mm diameter Zirconia rotors in an Ar-filled glovebox. High-resolution ^{7}Li MAS NMR spectra were acquired on a Varian InfinityPlus-500 MHz spectrometer at a magnetic field of 11.7 T, with a 1.3 mm MAS probe at a spinning speed of 50 kHz. Spectra were
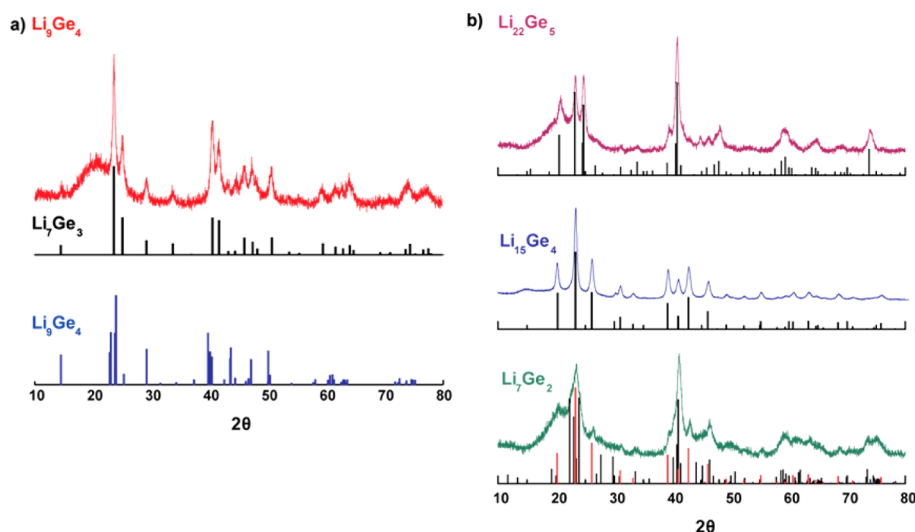
Figure 2. X-ray diffraction data (λ = 1.54 Å) for the phases obtained by high energy ball-milling with nominal stoichiometries: (a) Li_9Ge_4; (b) Li_7Ge_2, $Li_{15}Ge_4$, and $Li_{22}Ge_5$. The calculated peak intensities below each pattern correspond to the simulated patterns for the corresponding structures (with both Li_9Ge_4 and Li_7Ge_3 ($P3_21$) tick marks being shown for the "Li_9Ge_4" experimental pattern). The Li_7Ge_2 phase is not phase-pure and contains reflections from both the Li_7Ge_2 *Cmmm* structure (black; structure from DFT calculation[16]) and $Li_{15}Ge_4$ (red tick marks). The broad background centered at $2\theta = 20°$, most noticeable in the weaker patterns of the poorly crystalline phases, comes from the Kapton sample holder.

acquired using a rotor-synchronized spin−echo sequence (90°-τ-180°-τ-acq), where τ-values were set to be equal to one rotor period, i.e., 200 μs. The 90° pulse length was 2.2 μs and the recycle delay 10 s. ^{7}Li spectra were referenced to a 1 M ^{7}LiCl solution at 0 ppm. ^{7}Li MAS NMR spectra were normalized for analysis on the basis of the number of acquisitions and sample mass.

2.7. In-Situ ^{7}Li NMR. In-situ ^{7}Li experiments were carried out on a Tecmag Redstone 200 MHz spectrometer at a magnetic field of 4.7 T with a static probe. A one-pulse sequence with a 90° pulse length of 2 μs and a recycle delay of 10 s was used. ^{7}Li spectra were referenced to a 1 M ^{7}LiCl solution at 0 ppm. The Ge/Li battery was cycled at a rate of C/50.

3. RESULTS

3.1. Li_xGe_y Alloy Model Compounds. In order to facilitate accurate identification of chemical phases formed on cycling the Ge anodes, several previously reported Li_xGe_y alloys, Li_9Ge_4, Li_7Ge_2, $Li_{15}Ge_4$, and $Li_{22}Ge_5$, were prepared with high-energy ball-milling and characterized using powder XRD, PDF analysis, and *ex-situ* high-resolution ^{7}Li solid-state NMR spectroscopy.

3.1.1. X-ray Diffraction (XRD) and Pair Distribution Function (PDF) Analysis. XRD patterns of the materials with nominal compositions corresponding to the phases Li_9Ge_4, Li_7Ge_2, $Li_{15}Ge_4$, and $Li_{22}Ge_5$ are shown in Figure 2. Calculated PDFs with their fit to experimental data are found in Figure 3, and refinement statistics (residual values and phase fractions) are listed in Table 1.

The XRD reflections from $Li_{15}Ge_4$ can be indexed by the structure reported by Johnson et al.[31] This is further confirmed by the refinement against PDF data, which shows 70% $Li_{15}Ge_4$ with a 30% Li_7Ge_2 impurity that is not observed in the XRD pattern. That Li_7Ge_2 is not detected is unsurprising given the lack of crystallinity observed in the Li_7Ge_2 sample discussed below. The $Li_{22}Ge_5$ phase is also poorly crystalline, but Bragg reflections in the XRD pattern can be indexed by the structure reported by Gladyshevskii et al.[32] Refinement against PDF data shows an excellent fit, indicating that the model compound is composed of 89% $Li_{22}Ge_5$ with an 11% Li_7Ge_2 impurity.

The X-ray pattern of the phase with nominal composition Li_9Ge_4 bears little resemblance to the pattern for the reported *Cmcm* Li_9Ge_4 phase.[30] Instead, the pattern simulated from the phase Li_7Ge_3 (space group $P3_21$), identified by DFT calculations,[16] was a good match to the experimental data. A phase of this composition with the same space group has been previously mentioned in the literature, but no structural or characterization data was presented.[11] A second report of a phase with this composition suggested that Li_7Ge_3 adopted a rhombohedral space group ($R\bar{3}m$);[12] however, the DFT results[16] suggest that this rhombohedral phase most likely corresponds to Li_5Ge_2 or Li_8Ge_3: the simulated XRD patterns of Li_7Ge_3 (space group: $P3_21$) and Li_5Ge_2 (space group: $R\bar{3}m$) are similar, but the DFT results suggest that Li_7Ge_3 is a more stable phase.[16] The PDF pattern of this nominal Li_9Ge_4 phase (Figure 3) contains correlations characteristic of Ge−Ge dumbbells ($\sim$2.5 Å), and a broad shoulder at $\sim$2.8 Å, corresponding to the Li−Ge distances. Again, an extremely poor fit (R_w = 0.353) is obtained when a refinement using the Li_9Ge_4 structure is performed but a much improved fit (R_w = 0.183) is obtained when Li_7Ge_3 is used as an input to the structural refinement. The best fit to experimental data is obtained with a combination of 93% Li_7Ge_3 and 7% Li_9Ge_4, suggesting some slight disorder in the Li_7Ge_3 and/or the presence of a second minor phase. Our inability to prepare Li_9Ge_4 via ball-milling is consistent with the results from our prior calculations, which, based on the relative stabilities of the various phases, predict that Li_9Ge_4 should disproportionate to form the Li_7Ge_3 ($P3_21$) phase and a more Ge-rich phase.[16]

The PDF pattern of the nominal Li_7Ge_2 phase can be well modeled with phase fractions of 72% for Li_7Ge_2 (*Cmmm*) and 28% for $Li_{15}Ge_4$. Of note is the change in the cell c-parameter from 4.63 Å, reported by Hopf et al.,[28] to 4.49 Å (see Table S1). The reflections calculated from the model refined against the PDF data give a good match to the experimental XRD pattern (shown in Figure 2).

3.1.2. ^{7}Li Solid-State NMR. The characteristic NMR resonances for several Li_xGe_y model compounds are shown in Figure 4a. Reminiscent of the Li_xSi_y system,[18] the phases with
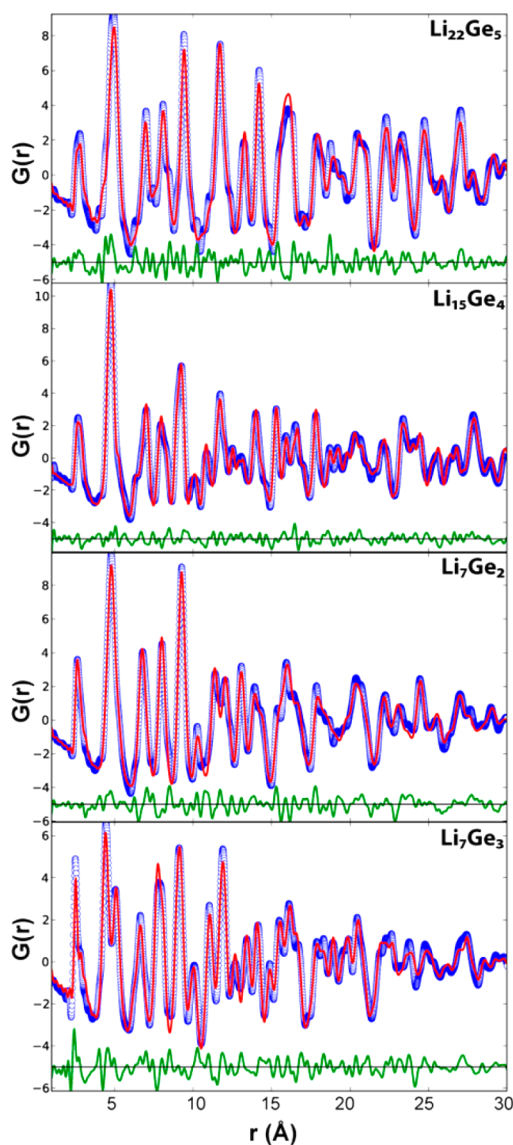
Figure 3. PDF $(G(r))$ patterns (blue) of the model compounds, Li_7Ge_3 (93% Li_7Ge_3 and 7% Li_9Ge_4), Li_7Ge_2 (72% Li_7Ge_2 and 28% of $Li_{15}Ge_4$), $Li_{15}Ge_4$ (70% $Li_{15}Ge_4$ and 30% Li_7Ge_2), and $Li_{22}Ge_5$ (89% $Li_{22}Ge_5$ and 11% Li_7Ge_2). Li_7Ge_3 ($Li_{2.33}Ge$) corresponds to the phase prepared with nominal composition Li_9Ge_4 ($Li_{2.25}Ge$). The refinement patterns are shown in red with green lines representing the difference between the experimental and refined patterns. Further details, including the chemical phases, their corresponding weighing factors, and refinement statistics, are shown in Table 1.

Table 1. Distribution of Ge in Different Phases in the Model Compounds with Corresponding R_w Values for the Fit to Experimental Data[a]
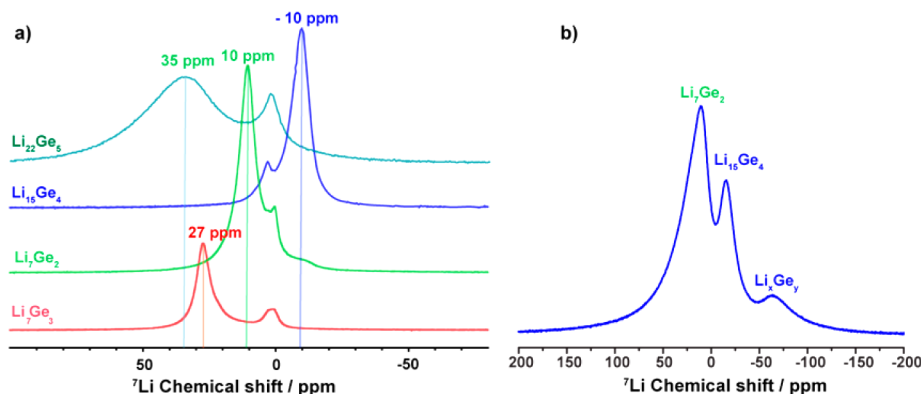
Nominal Composition	Phase 1	Phase 2	R_w
Li_9Ge_4	1 (Li_7Ge_3)	-	0.183
	0.93 (Li_7Ge_3)	0.07 (Li_9Ge_4)	0.175
Li_7Ge_2	1 (Li_7Ge_2)	-	0.178
	0.72 (Li_7Ge_2)	0.28 ($Li_{15}Ge_4$)	0.123
$Li_{15}Ge_4$	1 ($Li_{15}Ge_4$)	-	0.333
	0.70 ($Li_{15}Ge_4$)	0.30 (Li_7Ge_2)	0.085
$Li_{22}Ge_5$	1 ($Li_{22}Ge_5$)	-	0.203
	0.89 ($Li_{22}Ge_5$)	0.11(Li_7Ge_2)	0.183

[a]The relative abundance of each phase is determined from the unit cell content from the fits to PDF data.

The phase compositions of the synthesized Li_xGe_y model compounds obtained from PDF and NMR are mostly consistent, except that a noticeable discrepancy is observed for the nominal $Li_{15}Ge_4$ phase. The PDF analysis reveals that the $Li_{15}Ge_4$ phase actually contains more than 20% Li_7Ge_2, while NMR shows no obvious ^7Li resonance from Li_7Ge_2. The PDF measurements were acquired 2 weeks after the synthesis of $Li_{15}Ge_4$, while NMR experiments were carried out on a freshly prepared $Li_{15}Ge_4$ sample. In order to determine whether the samples transform over time, ^7Li MAS NMR was also carried out on the two-week old $Li_{15}Ge_4$ sample. The ^7Li NMR spectrum of aged $Li_{15}Ge_4$ (Figure 4b) now shows a dominant peak near 10 ppm, characteristic of Li_7Ge_2. In addition to the Li_7Ge_2 (10 ppm) and $Li_{15}Ge_4$ resonances (−10 ppm), another broad peak at −60 ppm suggests the formation of a Li-rich environment with a more shielded Li-environment than that found in $Li_{15}Ge_4$. Since no additional phase was observed in the PDF measurements, this suggests that this is a phase structurally related to $Li_{15}Ge_4$ (i.e., it has similar short-to-medium range environments) that cannot be clearly distinguished from $Li_{15}Ge_4$ in the PDF pattern. Two-dimensional ^7Li exchange NMR (Figure S4) shows that this Li-rich phase is close in space to the $Li_{15}Ge_4$ phase.

3.2. Electrochemical Studies of Micron-Sized Germanium Particles. *3.2.1. Electrochemistry.* Figure 5a shows the first discharge for micron-sized crystalline germanium vs Li metal down to 0 mV, with a current corresponding to C/50. The experimental discharge capacity of the first cycle is 1500 mAh/g. Four major processes are observed in the galvanostatic (Figure 5a) and differential capacity, dQ/dV, (Figure 5b) plots: an initial fast drop in potential to 350 mV, followed by two flatter regions, the first at around 350−250 mV and the second at around 200−150 mV, and finally a rapid drop to 0 V, with corresponding inflection points in the dQ/dV plot at 500, 350, 200, and 50 mV.

3.2.2. XRD. XRD patterns of lithiated Ge anodes obtained at different states of lithiation are shown in Figure 6. The pristine Ge electrode shows peaks corresponding to crystalline germanium ($Fd\bar{3}m$). These reflections broaden upon lithium insertion, suggesting the breakdown of the crystallites or increased disorder or strain.[39] (The line widths of the major Ge reflections for the pristine and 300 mV samples are tabulated in Table S2.) The reflections from the Ge phase decrease in intensity on lithiation, with a corresponding growth of the reflections from the $P3_21$ Li_7Ge_3 phase, with the reflections from this phase dominating in the 250 mV sample. Between 250 mV and 200 mV, Li_7Ge_3 transforms to a phase (or a group

lower lithium content and higher Ge−Ge connectivity (in this case, Ge dumbbells) resonate at higher frequencies, Li_7Ge_3 and Li_7Ge_2 giving rise to resonances at 27 and 10 ppm, respectively, while the more lithiated ones have resonances at lower frequencies, with $Li_{15}Ge_4$ resonating at −10 ppm. $Li_{22}Ge_5$ is metallic[18,36,37] and a Knight shift (instead of a chemical shift) results in +32 ppm. In addition to the major Li_xGe_y resonances, a peak is found in all the spectra at 2.8 ppm from Li_2O, the oxygen originating either from the surface oxide layers of the metal (Li and Ge) starting materials or from impurities introduced during the milling process. A minor Li_2CO_3 component may also be present due to reactions involving CO_2.[38]

Figure 4. (a) ^{7}Li MAS NMR spectra of the model compounds Li_7Ge_3, Li_7Ge_2, $Li_{15}Ge_4$, and $Li_{22}Ge_5$. Li_7Ge_3 ($Li_{2.33}Ge$) corresponds to the phase prepared with nominal composition Li_9Ge_4 ($Li_{2.25}Ge$). (b) ^{7}Li NMR spectrum of $Li_{15}Ge_4$ 2 weeks after synthesis. Chemical shifts of major isotropic resonances are marked in (a). The peaks close to 0 ppm correspond to diamagnetic (oxygen-containing) impurities. Li_xGe_y refers to a Li-rich phase that results from the decomposition of $Li_{15}Ge_4$.
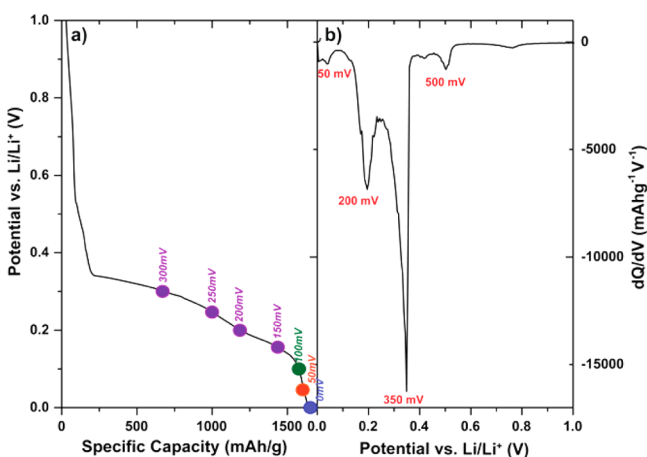
Figure 5. Electrochemistry plots, potential vs capacity (a), and the differential capacity dQ/dV (b) of a Ge/Li battery obtained at a discharge rate of C/50. The filled circles designate the states of charge of the discharged electrodes disassembled for *ex-situ* XRD, PDF, and NMR characterization as shown in Figures 6, 7, and 8, respectively.
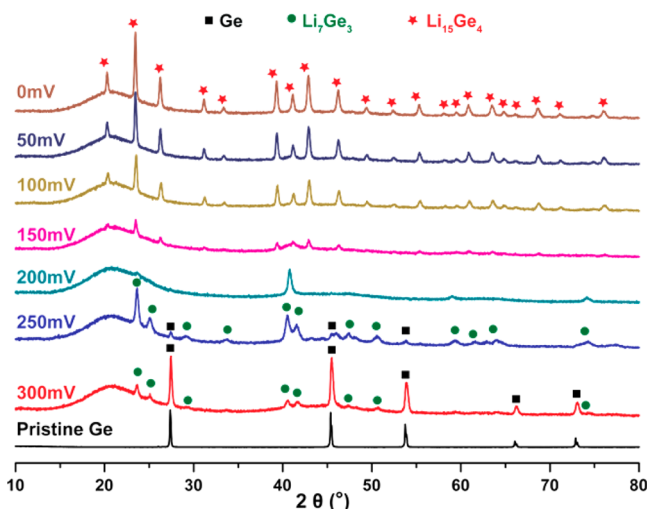

Figure 6. *Ex-situ* XRD patterns ($\lambda = 1.54$ Å) of cycled Ge electrodes obtained at the various stages of lithation marked in Figure 5, with corresponding potentials vs Li/Li$^+$ indicated. Major reflections from Ge (■), Li_7Ge_3 (green circles), and $Li_{15}Ge_4$ (red stars) are marked.

of phases) with a major, intense, broad reflection at $2\theta = 41°$ and three minor ones at 24°, 59°, and 74° ($\lambda = 1.54$ Å). These four reflections are found in the diffraction pattern of the Li_7Ge_2 model compound (a comparison is shown in Figure S2), but other Li_7Ge_2 reflections are missing, indicating that the phase formed is not crystalline Li_7Ge_2. Further lithiation beyond 200 mV leads to the formation of crystalline $Li_{15}Ge_4$. The reflections from $Li_{15}Ge_4$ continue to grow stronger until the end of discharge at 0 mV. A reduction in the full width at half-maximum (FWHM; Table S3) of all the $Li_{15}Ge_4$ reflections suggests increased crystallinity. There is no evidence of $Li_{22}Ge_5$ or any other more highly lithiated phase. Le Bail refinements of XRD patterns of lithiated Ge anodes at 100, 50, and 0 mV (Figure S3 and Table S4) show gradually increased unit cell parameters, suggesting that the $Li_{15}Ge_4$ phase is able to accommodate a range of lithium stoichiometries and that the final lithiation product may contain additional lithium beyond the composition $Li_{15}Ge_4$ (or $Li_{3.75}Ge$).

3.2.3. PDF. Experimental PDF patterns, obtained at various stages of lithiation, are shown in Figure 7. Visual analysis of the PDFs provides atomic-scale insights into the changes occurring on lithiation. The PDF for the pristine material shows sharp correlations out to high-r values (>100 Å). On initial lithiation, the peaks broaden significantly and the r_{max} (the maximum distance at which features are observed in the PDF) reduces to around 40 Å, indicating a loss in correlation length consistent with broadening of Bragg peaks in the XRD. The reduction in r_{max} continues to 150 mV, where significant correlations are observed only to approximately 20 Å. At further lithiation, peaks sharpen significantly, indicating the crystallization of phases at the end of lithiation.

Peaks corresponding the Ge-connectivity are clearly visible in the PDF and are signatures of the Ge−Ge building units that are present. The sharp peak at 2.5 Å seen in the PDF of the pristine electrode is characteristic of Ge−Ge bonds. A new broad peak at ~2.7 Å from Li−Ge correlations grows as a shoulder to the right of the Ge−Ge peak. Two other peaks at 3.8 and 4.4 Å from Ge−Ge next-nearest neighbor correlations in crystalline Ge shift to larger values between 300 and 250 mV, indicating an increase in Ge−Ge distances due to the insertion of Li and the breakdown of the extended Ge-framework. The Ge−Ge peaks broaden upon further lithiation, the broading of the peaks in the 200 mV data suggesting that the material is highly disordered in this voltage region. At 150 mV, the 2.5 Å
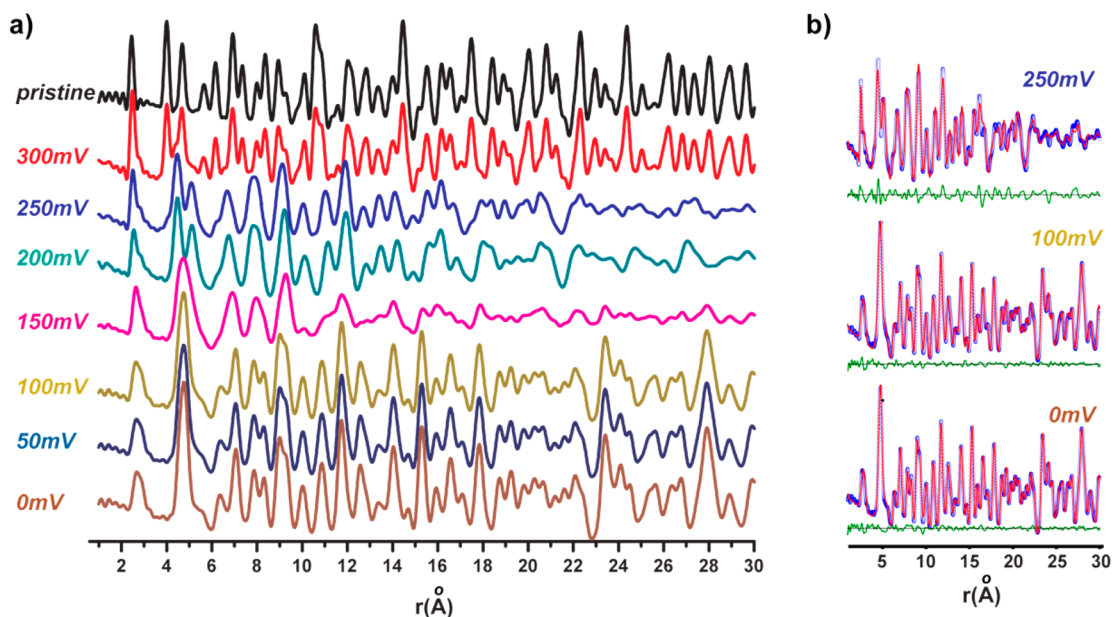
Figure 7. (a) PDF patterns of cycled Ge electrodes at the different states of charge shown in Figure 5, with corresponding potentials vs Li/Li+ indicated. (b) Representative refinements (red) overlapped with experimental patterns (blue) at 250, 100, and 0 mV. The difference between the experimental and simulated PDF is shown in green. The phase compositions extracted from the refinement results, at each state of charge, are listed in Table 2.

Table 2. Germanium Phases Obtained Following Discharging against Lithium to Different Voltage Cutoffs, with the Corresponding R_w Values[a]

	Li content	Ge	Li_7Ge_3	$Li_{13}Ge_5$	$Li_{13}Ge_4$	Li_7Ge_2	$Li_{15}Ge_4$	R_w
300 mV	1.6	0.66	0.34					0.2090
250 mV	2.5	0.06	0.94					0.1180
200 mV	3.1			0.81	0.19			0.1570
				0.76		0.24		0.1790
150 mV	3.9					0.76	0.24	0.1260
100 mV	4.0		0.13				0.87	0.0603
50 mV	3.9		0.11				0.89	0.0599
0 mV	4.1					0.04	0.96	0.0618

[a]The relative abundance of each Ge-containing phase was normalized based on the number of Ge atoms per unit cell.

peak is barely visible and a broad correlation is observed at 4.7 Å, characteristic of the first Ge−Ge nonbonded distance in Li_7Ge_2 and $Li_{15}Ge_4$, indicating that the majority of Ge is present as isolated atoms. The 4.7 Å peak sharpens at lower voltages, indicating that the end product of this phase transition contains a narrower range of Ge−Ge (first shell, nonbonded) distances indicative of increased crystallinity, as observed in the XRD.

The germanium phase distribution was quantified by performing least-squared refinements against the PDF data. Representative refinements of the PDF patterns at 250, 100, and 0 mV are shown in Figure 7b (full refinement patterns and refinement statistics can be found in Figure S5 and Table S5), and the phase compositions at different states of charge from the refinement results are summarized in Table 2. Refinement of a Ge-model structure against PDF data gives a good fit, with relatively few changes to structural parameters. The initial insertion of Li converts Ge into Li_7Ge_3, and at 300 mV, there is already a significant fraction (0.34) of Li_7Ge_3 present. Of note is the presence of an amorphous phase (additional to Ge and Li_7Ge_3) at early stages of the lithiation (Figure S5), characterized by a sharp peak at 2.55 Å (slightly longer than the Ge−Ge distance in crystalline Ge) and a second broad peak at 4.4 Å (Figure S7, Table S9). Addition of a second Li_7Ge_3

phase of particle diameter 6.7 Å is able to model this feature well, and reduces the R_w of the refinement from 20.9% to 11.5%. We believe that this phase consists of short-range ordered areas of Ge−Ge dumbbells within or on the surface of the largely crystalline Ge-matrix, which form as a result of lithium incorporation into the crystalline Ge structure on initial lithiation and act as nucleation points for the growth of Li_7Ge_3. The connectivity of this phase is certainly different from that of reported forms of amorphous-Ge, which have been found by neutron PDF to consist of a disordered tetrahedral network.[40] Complete conversion to Li_7Ge_3 occurs at 250 mV. This phase is assigned to Li_7Ge_3 as opposed to Li_5Ge_2 (a phase with a similar Li:Ge ratio (2.33 vs 2.5) that gives rise to an almost indistinguishable XRD pattern) on the basis of the larger thermal parameters obtained in refinements using the Li_5Ge_2 phase, which suggest that a higher degree of disorder in the atomic positions is required to capture the information in the PDF (Figure S6 and Table S8), and the higher R_w value. In addition, the DFT calculations[16] predict that Li_7Ge_3 is the stable phase around this composition; Li_5Ge_2 is metastable.

The best fit to the PDF pattern at 200 mV with a single known or theoretically predicted[16] phase is obtained when the phase $Li_{13}Ge_5$ ($Li_{2.6}Ge$), comprising Ge−Ge dumbbells and

isolated Ge, was used; this phase is predicted to be thermodynamically stable.[16] The addition of a second phase, $Li_{13}Ge_4$ ($Li_{3.25}Ge$), also containing Ge−Ge dumbbells and isolated Ge, improves the fitting quality (R_w is reduced from 0.249 to 0.157). Several two-phase combinations of Li_xGe_y phases (including Li_5Ge_2, $Li_{13}Ge_5$, Li_8Ge_3, $Li_{13}Ge_4$, and Li_7Ge_2 ($Cmmm$)) can fit the data without significantly compromising the quality of the refinement, however, the best quality fits were always obtained when one of the components was $Li_{13}Ge_5$. The refinement data with various one-phase or two-phase combinations can be found in Tables 2 and S6. The common structural feature of all these compounds is parallel-aligned Ge−Ge dumbbells with discrete Li and in some cases Ge atoms in-between, as discussed below.

$Li_{15}Ge_4$ is observed at 150 mV along with residual Li_7Ge_2. Correlations from crystalline $Li_{15}Ge_4$ dominate the PDF pattern until the end of discharge, with the correlations persisting out to more than 70 Å. The presence of minor Li_7Ge_3 or Li_7Ge_2 components (<10% phase fraction) may result from the decomposition of metastable $Li_{15}Ge_4$ or may simply be a signature of residual Ge−Ge dumbbell-containing phases due to the inhomogeneous nucleation of the $Li_{15}Ge_4$ phase from these disordered phases, as is seen for lithiation of Si.[33] (The R_w is reduced from 0.0686 to 0.0618 for the 0 mV sample on inclusion of these minor phases in the refinement.)

3.2.4. Ex-Situ ^7Li NMR. Ex-situ ^7Li solid-state MAS NMR provides insight into the lithium local environments formed on lithiation (Figure 8). ^7Li resonances at around ∼0 ppm,
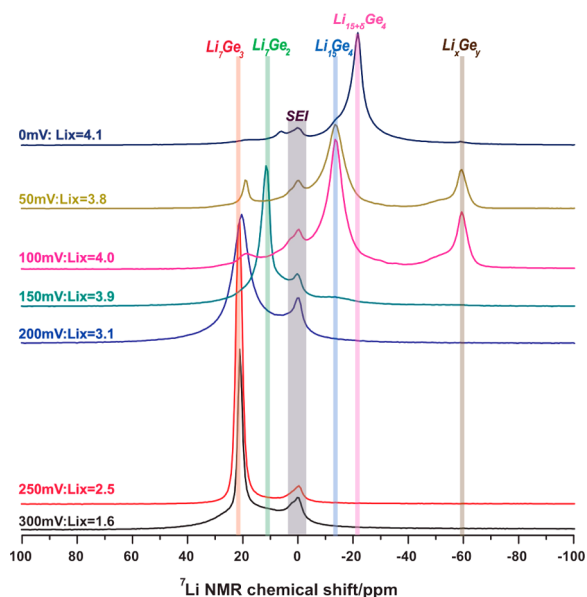
Figure 8. *Ex-situ* ^7Li NMR spectra (normalized) of cycled Ge electrodes at the states of charge identified in Figure 5a, with corresponding potentials vs Li/Li$^+$ and Li content indicated. Relevant peak assignments are shown. Li_xGe_y refers to a Li-rich phase that results from the decomposition of $Li_{15}Ge_4$.

characteristic of the formation of the solid-electrolyte-interphase (SEI) phase, are observed at the early stages of discharge (300 mV), presumably due to the decomposition of electrolyte solvents (EC and DMC) on the carbon and Ge anode surfaces.[26,41] A sharp resonance at ∼22 ppm also appears, an indication of the presence of the Li_7Ge_3 phase. The broader component under the 22 ppm resonance is tentatively

ascribed to lithium ions present in the crystalline Ge phase and possibly the formation of more disordered lithiated Ge phases. PDF refinements also suggest the presence of an additional amorphous phase containing short-range ordered Ge−Ge dumbbells in this voltage region. At 250 mV, the Li_7Ge_3 resonance dominates the spectrum and the broad component has essentially disappeared. The "Li_7Ge_3" resonance grows further but has also broadened significantly and shifted slightly to a lower chemical shift value for the sample obtained at 200 mV, suggesting a distribution of Li local environments, consistent with the disorder observed in both the XRD and PDF patterns. The lower shift is consistent with the PDF data, which indicated that $Li_{13}Ge_5$ ($Li_{2.6}Ge$) was present as a major component at this point, with further lithiation and the breakage of Ge−Ge bonds all resulting in smaller ^7Li chemical shifts. At 150 mV, a single, sharp resonance is observed at 10 ppm, characteristic of Li_7Ge_2. Upon further lithiation, Li_7Ge_2 is converted to $Li_{15}Ge_4$ (−13 ppm). Two additional peaks are observed, a minor resonance at around 20 ppm (likely from Li_7Ge_3 or phases containing similar ^7Li local environments to those found in Li_7Ge_3), consistent with the PDF analysis, and a peak at −58 ppm. This −58 ppm peak is also found in the ^7Li NMR spectra of the model compound $Li_{15}Ge_4$ 2 weeks after its synthesis, possibly a decomposition product of $Li_{15}Ge_4$. 2D exchange NMR (Figure S4) reveals that this −58 ppm phase is in close proximity to $Li_{15}Ge_4$ on the nanoscale, suggesting the decomposition product is in the same phase as $Li_{15}Ge_4$ or on the surface of $Li_{15}Ge_4$. Lithiation of the Ge anode to 0 mV results in a ^7Li resonance at −22 ppm, which is ascribed to an overlithiated phase $Li_{15+\delta}Ge_4$, similar to the process observed in the lithiation Si anodes ($Li_{15+\delta}Si_4$) in our prior studies.[18,33]

3.2.5. In-Situ ^7Li NMR. In-situ ^7Li NMR was performed to understand the sequential events occurring during the lithiation process further. The advantage of this method is that the battery is not stopped during the experiment, which removes the possibility of structural relaxation of metastable phases when the voltage is removed and any possible decomposition of the products that may occur over time and before the sample is investigated in the *ex-situ* experiment.[18] The spectra (Figure 9) all show an intense peak around 0 ppm, from the free electrolyte in the bag cell and SEI on the surface of the electrode. No other discernible, well-defined signal is observed at voltages above 300 mV. A broad component with a shift of ∼23 ppm, assigned to Li_7Ge_3, starts to appear below 300 mV. This resonance progressively grows in intensity and sharpens until potentials below 200 mV are reached; this corresponds to the flatter voltage region between 350 mV and approximately 200 mV in the electrochemical curve. Below 200 mV, the 23 ppm resonance continuously shifts to around 10 ppm, the shift observed in the model compound Li_7Ge_2. This suggests a continuous structural transformation from Li_7Ge_3 to Li_7Ge_2. A weak and broad resonance starts to grow in at around −13 ppm (overshadowed by the strong electrolyte peak at 0 ppm) around 150 mV, consistent with the formation of $Li_{15}Ge_4$. Deeper discharge to 0 mV leads to an intense peak at −22 ppm, likely from an overlithiated phase $Li_{15+\delta}Ge_4$.

4. DISCUSSION

On the basis of the electrochemistry, XRD, PDF, and *in-/ex-situ* NMR analyses, we propose a four-step mechanism for the lithiation process of micron-sized Ge particles:

i. OCV to 350 mV: Formation of an SEI Layer. Lithiation of Ge anodes starts with a steep drop in voltage to 350 mV,
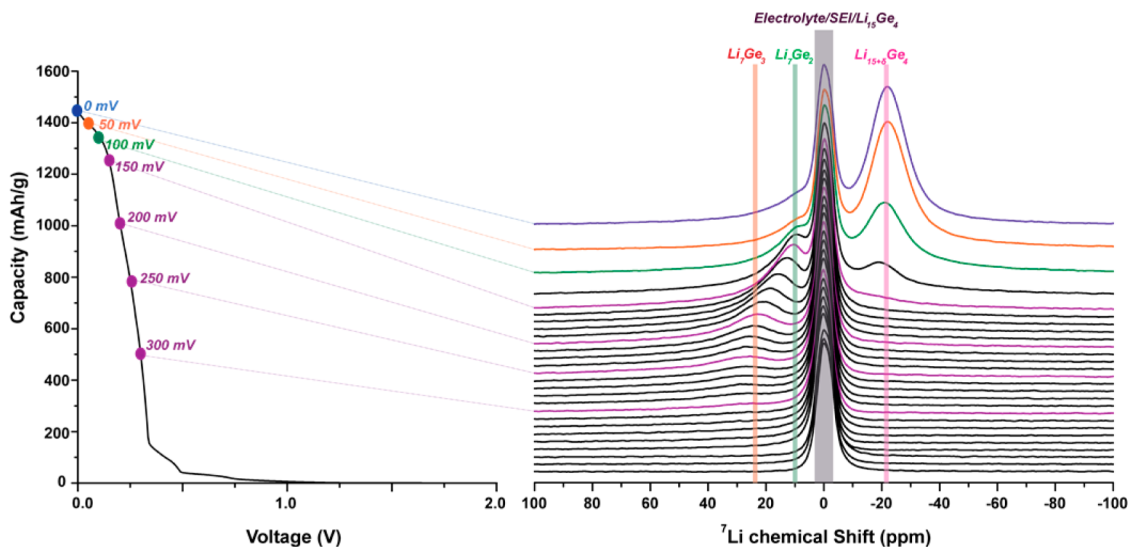
Figure 9. *In-situ* ^{7}Li NMR spectra of a Ge/Li plastic-bag battery cycled at a rate of C/50. The corresponding states of charge for select spectra are indicated on the electrochemical profile. Possible assignments to specific chemical phases are indicated.

with a small inflection appearing at 500 mV in the electrochemistry profile. The capacity (<0.5 Li) obtained in this region is mainly from electrolyte decomposition to form an SEI layer on the surfaces of Ge/C (with evidence from the ^{7}Li peak at close to 0 ppm in the *ex-situ* NMR), the insertion of Li within crystalline Ge, and possibly the reaction with GeO_2 impurities on the surface of Ge.

ii. 350 mV to 250 mV: Conversion from Crystalline Ge to Li_7Ge_3. A flatter voltage region is observed in the electrochemistry. Nominally, a two-phase reaction mechanism is observed in this voltage regime, as indicated by the coexistence of both Ge and Li_7Ge_3 phases, in the XRD and PDF patterns of the 300 and 250 mV samples. A single main resonance at 22−23 ppm from the Li_7Ge_3 phase in the *in-/ex-situ* NMR spectra with little variation in the shift position also supports a two-phase reaction mechanism. The potential should be completely flat for a two-phase reaction, the sloping potential profile being associated with the difficulty in breaking up the crystalline Ge lattice, resulting in a considerable overpotential. This is similar to that observed for Si.[42,43] A recent *in-situ* XRD and XAS study[23] showed an abrupt decrease of the crystalline Ge phase between 253 mV and 210 mV. These authors attribute the change to the two-phase reaction from crystalline-Ge to amorphous Li_9Ge_4, the Ge−Ge distances in the EXAFS resembling those of Li_9Ge_4 at 253 mV. In contrast, our XRD and PDF analyses clearly show that $Li_7Ge_3(P32_12)$, not Li_9Ge_4 forms, with Li_7Ge_3 being the stable phase at and close to this composition, on the basis of DFT calculations.[16] These phases are difficult to distinguish using techniques such as EXAFS. Both Li_9Ge_4 and Li_7Ge_3 contain Ge−Ge dumbbells, but with different spacings (or numbers of Li) between the dumbbells and slightly longer Ge−Ge dumbbell bond lengths in Li_7Ge_3. We note also that our studies were performed at a slower rate (C/50 vs C/15[23]), which may influence the nature and crystallinity of the phases that are formed.

iii. 250 mV to 150 mV: Structural Transformation from Li_7Ge_3 to Li_7Ge_2. A gradual sloping voltage region is observed in the electrochemistry. The continuous shift of the ^{7}Li resonance in the *in-situ* spectra implies a continuous structural transformation from Li_7Ge_3 to local structures resembling

Li_7Ge_2. The broad ^{7}Li resonances seen in the *ex-situ* NMR experiments also suggest a greater degree of local disorder compared with other regions. Both the XRD and PDF patterns also indicate considerable disorder. Nonetheless, broad Bragg reflections are still observed, indicating the existence of partial ordering along certain directions. PDF refinements suggest that specific short-range structural motifs—columns containing Ge−Ge dumbbells and isolated Ge/Li atoms—are formed in this region. These are present in all the following phases, Li_7Ge_3, Li_5Ge_2, $Li_{13}Ge_5$, Li_8Ge_3, and $Li_{13}Ge_4$ as shown in Figure 10, but refinement indicates that none of these phases is the sole lithiation product.

Combining the evidence from XRD, PDF, and NMR, the lithiation process at this stage likely follows a heterogeneous
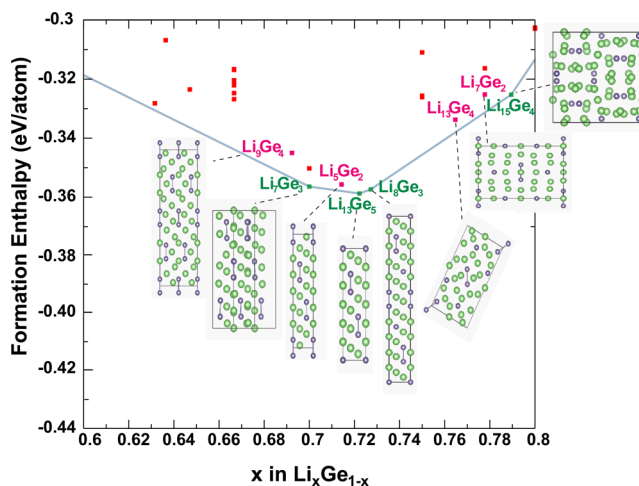
Figure 10. Lithiation pathway showing the common structural features of possible lithiated Ge phases between Li_9Ge_4 and Li_7Ge_2: they all contain parallel-aligned Ge−Ge dumbbells in columns with discrete Li and in some cases Ge atoms in-between them. The $Li_{15}Ge_4$ phase with isolated Ge atoms is shown for comparison. The blue line is the tie-line indicating the stable phases at 0 K predicted by DFT.[16] The squares indicate the formation enthalpy of a structure: green squares correspond to the thermodynamic phases; red squares correspond to metastable phases (at 0 K).

pathway from Li_7Ge_3 (Ge−Ge bond length: 2.50 Å) to Li_7Ge_2 (Ge−Ge bond length: 2.62 Å), via Li_5Ge_2, $Li_{13}Ge_5$, Li_8Ge_3, and $Li_{13}Ge_4$, where the common structural features of all these phase are maintained. Ge−Ge bonds are gradually broken, and the fraction of Li and isolated Ge atoms increases, so that by 150 mV, Li_7Ge_2 dominates. Lim et al.[23] also suggested that the Ge−Ge bond distances increase to 2.6 Å below 220 mV, consistent with the proposed formation of Li_7Ge_2. As shown in Figure 10, $Li_{13}Ge_4$ and Li_7Ge_2 lie above the convex hull (i.e., they are metastable phases). Their formation is, therefore, kinetically driven: the system reacts to form structural motifs that locally resemble $Li_{13}Ge_4$ and Li_7Ge_2 rather than forming $Li_{15}Ge_4$ directly from the thermodynamic phases $Li_{13}Ge_5$ and Li_8Ge_3; only when the Ge−Ge bonds are weak enough/present in too low concentrations is the growth of the $Li_{15}Ge_4$ crystalline phase kinetically favored.

iv. 150 mV to 0 mV: Transformation from Li_7Ge_2 to $Li_{15}Ge_4$ and Overlithiated $Li_{15}Ge_4$. A steep drop in voltage is observed in the electrochemistry. The appearance of sharp reflections in the XRD patterns and long-range correlations in PDF indicates the relatively high crystallinity of the $Li_{15}Ge_4$ phase. Some Li_7Ge_3 and a Li-rich phase are seen in the ex-situ PDF and NMR experiments, which we ascribe to the decomposition of the $Li_{15}Ge_4$ phase before the experiments are performed or a certain degree of inhomogeneity in the lithiation process. The formation of $Li_{15}Ge_4$ from the metastable Li_7Ge_2 phase is similar to what is observed in silicon anodes; however, here, the Si−Si bonds within an amorphous (rather than partially ordered) phase need to be broken before the $Li_{15}Si_4$ phase nucleates. In a further analogy with the Si chemistry, subsequent lithiation leads to the formation of an overlithiated phase, which shows a different Li local environment in the ^7Li NMR spectra as compared with $Li_{15}Ge_4$. This overlithiated phase shares a similar long-/short-range structure as $Li_{15}Ge_4$, as suggested by the lack of significant change in the XRD or PDF patterns other than an increased unit cell parameter (from 10.7232(3) Å to 10.7479(2) Å). We, thus, tentatively assign this overlithiated phase to $Li_{15+\delta}Ge_4$, its formation presumably being associated with the 50 mV process seen electrochemically. (The same process for silicon occurs at essentially the same potential; however, in the silicon case, it is more difficult to separate $Li_{15}Si_4$ formation from its overlithiation due to the larger kinetic barrier for crystalline $Li_{15}Si_4$ formation and the larger overpotential typically required to drive the reaction.[18,33]) No indication of $Li_{22}Ge_5$, as proposed by some prior studies,[27] is found; even at the very end of discharge, the $Li_{22}Ge_5$ phase possesses distinctive signatures in both the NMR spectra and PDF patterns.

Finally, we note that the nature of the phases depends somewhat on the size of Ge nanoparticles and the lithiation rates, both of which will alter the kinetics of the various phase transformations. For example, Yoon et al. have observed noticeable differences in the voltages of the various processes depending on the particle size and nature of the carbon wiring.[27] The disordered (250−150 mV) region will be particularly sensitive to lithiation rates and particle sizes, since there are numerous structurally related phases with very similar energies. In addition, variations in potentials across the electrode (due to differences in electronic wiring, tortuosities of the paths for Li^+ in the electrolyte) will all affect which phases are formed during the lithiation process.

Amorphous Ge has been shown previously to form on charging (delithation).[23,44] By analogy with previous studies of Si, where a lower overpotential was observed for Si−Si bond breakage in amorphous Si vs crystalline Si,[19] lithiation in subsequent cycles may occur at a lower overpotential, which may impact the phases that are observed. Importantly, however, this work provides a structural basis with which to interpret subsequent cycles. Indeed, our preliminary studies indicate that a similar lithiation pathway occurs in subsequent cycles with the reformation of the Li_7Ge_3 phase that is reported in this paper; a further study of the delithiation process and the structural transformations that occur in subsequent cycles will be reported in future papers.

5. CONCLUSIONS

The lithiation mechanisms of micron-sized Ge anodes have been studied with XRD, PDF, and in-/ex-situ high-resolution ^7Li solid-state NMR spectroscopy. Relevant model compounds identified in previous studies, i.e. Li_9Ge_4, Li_7Ge_2, $Li_{15}Ge_4$, and $Li_{22}Ge_5$, were first synthesized and characterized to provide experimental signatures for identifying Li_xGe_y phases in lithiated Ge products. Li_9Ge_4 was not formed under the synthetic conditions used in this work. Instead, the $P32_12$ polymorph of Li_7Ge_3 was formed, a phase that has been predicted to be thermodynamically stable in our prior DFT calculations[16] but had not unambiguously been identified experimentally.

The lithiation process of micron-sized Ge anodes involves the formation of the Li_7Ge_3 phase initially through a two-phase reaction process. No Li_9Ge_4 was formed, contrary to some previous reports. Interestingly, Li_7Ge_3 converts to Li_7Ge_2 via a series of highly disordered phases; as shown in Figure 10, all of these phases contain columns of Li, Ge−Ge, and Ge, with the relative proportions varying as lithiation proceeds. Eventually, Li_7Ge_2-like short-to-medium range environments are observed (by NMR and PDF analysis), indicating that most of the Ge−Ge bonds have been broken. At this point, the nucleation and growth to form crystalline $Li_{15}Ge_4$ occurs. This phase can be further lithiated, likely to form $Li_{15+\delta}Ge_4$.

In conclusion, this study provides a compelling illustration of how a variety of ex-/in-situ, experimental techniques which probe short-, medium-, and long-range structure in combination with structural and energetic predictions from DFT studies can be used to obtain comprehensive insights into complex lithiation mechanisms in alloy phases. In particular, DFT studies identified a stable polymorph for the composition Li_7Ge_3, which was then shown by experiments to represent a key structure on the lithiation pathway.

■ ASSOCIATED CONTENT

Ⓢ Supporting Information

Details of XRD analysis, 2D NMR results, and PDF results. This material is available free of charge via the Internet at http://pubs.acs.org.

■ AUTHOR INFORMATION

Corresponding Author
*E-mail: cpg27@cam.ac.uk.

Present Address
Y.-Y.H.: Department of Chemistry & Biochemistry, Florida State University, Tallahassee, Florida 32306.

Notes

The authors declare no competing financial interest.

■ REFERENCES

(1) Kim, T. H.; Park, J. S.; Chang, S. K.; Choi, S.; Ryu, J. H.; Song, H. K. *Adv. Energy Mater.* **2012**, *2*, 860.
(2) Park, C. M.; Kim, J. H.; Kim, H.; Sohn, H. J. *Chem. Soc. Rev.* **2010**, *39*, 3115.
(3) Obrovac, M. N.; Christensen, L. *Electrochem. Solid-State Lett.* **2004**, *7*, A93.
(4) Seng, K. H.; Park, M. H.; Guo, Z. P.; Liu, H. K.; Cho, J. *Nano Lett.* **2013**, *13*, 1230.
(5) Zhang, W.-J. *J. Power Sources* **2011**, *196*, 13.
(6) Fuller, C.; Ditzenberger, J. *Phys. Rev.* **1953**, *91*, 193.
(7) Wang, D. W.; Chang, Y. L.; Wang, Q.; Cao, J.; Farmer, D. B.; Gordon, R. G.; Dai, H. J. *J. Am. Chem. Soc.* **2004**, *126*, 11602.
(8) Li, D.; Seng, K. H.; Shi, D.; Chen, Z.; Liu, H. K.; Guo, Z. *J. Mater. Chem. A* **2013**, *1*, 14115.
(9) Sangster, J.; Pelton, A. D. *J. Phase Equilib.* **1997**, *18*, 289.
(10) Grüttner, A.; Nesper, R.; Von Schnering, H. G. *Angew. Chem., Int. Ed.* **1982**, *21*, 912.
(11) Grüttner, A.; Nesper, R.; Von Schnering, H. G. *Acta Crystallogr.* **1981**, *A37* (Suppl), C.
(12) Jain, A.; Kawasako, E.; Miyaoka, H.; Ma, T.; Isobe, S.; Ichikawa, T.; Kojima, Y. *J. Phys. Chem. C* **2013**, *117*, 5650.
(13) Dupke, S.; Langer, T.; Pottgen, R.; Winter, M.; Eckert, H. *Solid State Nucl. Mag.* **2012**, *42*, 17.
(14) Pickard, C. J.; Needs, R. J. *Phys. Rev. Lett.* **2006**, *97*, 045504.
(15) Pickard, C. J.; Needs, R. J. *J. Phys.: Condens. Matter* **2011**, *23*, 053201.
(16) Morris, A. J.; Grey, C. P.; Pickard, C. J. *Phys. Rev. B: Condens. Matter Mater. Phys.* **2014**, *90*, 054111.
(17) St. John, M. R.; Furgala, A. J.; Sammells, A. F. *J. Electrochem. Soc.* **1980**, *127*, C136.
(18) Key, B.; Bhattacharyya, R.; Morcrette, M.; Seznéc, V.; Tarascon, J.-M.; Grey, C. P. *J. Am. Chem. Soc.* **2009**, *131*, 9239.
(19) Key, B.; Morcrette, M.; Tarascon, J.-M.; Grey, C. P. *J. Am. Chem. Soc.* **2010**, *133*, 503.
(20) Kim, Y.; Hwang, H.; Lawler, K.; Martin, S. W.; Cho, J. *Electrochim. Acta* **2008**, *53*, 5058.
(21) Baggetto, L.; Notten, P. H. L. *J. Electrochem. Soc.* **2009**, *156*, A169.
(22) Liu, X. H.; Liu, Y.; Kushima, A.; Zhang, S.; Zhu, T.; Li, J.; Huang, J. Y. *Adv. Energy Mater.* **2012**, *2*, 722.
(23) Lim, L. Y.; Liu, N.; Cui, Y.; Toney, M. F. *Chem. Mater.* **2014**, *26*, 3739.
(24) Hatchard, T. D.; Dahn, J. R. *J. Electrochem. Soc.* **2004**, *151*, A838.
(25) Li, J.; Dahn, J. R. *J. Electrochem. Soc.* **2007**, *154*, A156.
(26) Graetz, J.; Ahn, C. C.; Yazami, R.; Fultz, B. *J. Electrochem. Soc.* **2004**, *151*, A698.
(27) Yoon, S.; Park, C.-M.; Sohn, H.-J. *Electrochem. Solid-State Lett.* **2008**, *11*, A42.
(28) Hopf, V.; Müller, W.; Schäfer, H. *Z. Naturforsch., B: Chem. Sci.* **1972**, *27*, 1157.
(29) Gladyshevskii, E. I.; Oleksiv, G. I.; Kripyake, P. I. *Sov. Phys. Crystallogr.* **1964**, *9*, 269.
(30) Hopf, V.; Schäfer, H.; Weiss, A. *Z. Naturforsch., B: Chem. Sci.* **1970**, *25*, 653.
(31) Johnson, Q.; Smith, G. S.; Wood, D. *Acta Crystallogr.* **1965**, *18*, 131.
(32) Gladyshevskii, E. L.; Oleksiv, G. I.; Kripyakevich, P. I. *Sov. Phys. Crystallogr.* **1964**, *9*, 269.
(33) Ogata, K.; Salager, E.; Kerr, C. J.; Fraser, A. E.; Ducati, C.; Morris, A. J.; Hofmann, S.; Grey, C. P. *Nat. Commun.* **2014**, *5*, 3217.
(34) Wang, X. L.; Han, W. Q.; Chen, H.; Bai, J.; Tyson, T. A.; Yu, X. Q.; Wang, X. J.; Yang, X. Q. *J. Am. Chem. Soc.* **2011**, *133*, 20692.
(35) Farrow, C. L.; Juhás, P.; Liu, J. W.; Bryndin, D.; Božin, E. S.; Bloch, J.; Proffen, T.; Billinge, S. J. L. *J. Phys.: Condens. Matter* **2007**, *19*, 335219.
(36) Bekaert, E.; Robert, F.; Lippens, P. E.; Ménétrier, M. *J. Phys. Chem. C* **2010**, *114*, 6749.
(37) Schäfer, H.; Eisenmann, B.; Müller, W. *Angew. Chem., Int. Ed.* **1973**, *12*, 695.
(38) Mosqueda, H. A.; Vazquez, C.; Bosch, P.; Pfeiffer, H. *Chem. Mater.* **2006**, *18*, 2307.
(39) Ungár, T. *Scr. Mater.* **2004**, *51*, 777.
(40) Walters, J. K.; Newport, R. J. *Phys. Rev. B: Condens. Matter Mater. Phys.* **1996**, *53*.
(41) Chan, C. K.; Zhang, X. F.; Cui, Y. *Nano Lett.* **2007**, *8*, 307.
(42) Obrovac, M. N.; Christensen, L. *Electrochem. Solid-State Lett.* **2004**, *7*, A93.
(43) Jamnik, J.; Maier, J. *Phys. Chem. Chem. Phys.* **2003**, *5*, 5215.
(44) Jia, H.; Kloepsch, R.; He, X.; Badillo, J. P.; Gao, P.; Fromm, O.; Placke, T.; Winter, M. *Chem. Mater.* **2014**, *26*, 5683.